JACS
JOURNAL OF THE AMERICAN CHEMICAL SOCIETY
pubs.acs.org/JACS
Article

Conductive Covalent Organic Frameworks of Polymetallophthalocyanines as a Tunable Platform for Electrocatalysis

Yi Zhang, Xiyuan Zhang, Long Jiao, Zheng Meng,* and Hai-Long Jiang*

Cite This: J. Am. Chem. Soc. 2023, 145, 24230−24239
Read Online

ABSTRACT: Developing an electrocatalyst platform that can control the interplay among activity, selectivity, and stability at atomic precision remains a grand challenge. Here, we have synthesized highly crystalline polymetallophthalocyanines (*p*MPcs, M = Fe, Co, Ni, and Cu) through the annulation of tetracyanobenzene in the presence of transition metals. The conjugated, conductive, and stable backbones with precisely installed metal sites render *p*MPcs a unique platform in electrochemical catalysis, where tunability emerges from long-range interactions. The construction of *p*CoNiPc with a Co and Ni dual-site integrates the advantageous features of *p*CoPc and *p*NiPc in electrocatalytic CO_2 reduction through electronic communication of the dual-site with an unprecedented long atomic separation of ≥14 chemical bonds. This integration provides excellent activity (current density, $j = -16.0$ and -100 mA cm^{-2} in H-type and flow cell, respectively), selectivity (CO Faraday efficiency, $FE_{CO} = 94\%$), and stability (>10 h), making it one of the best-performing reticular materials.

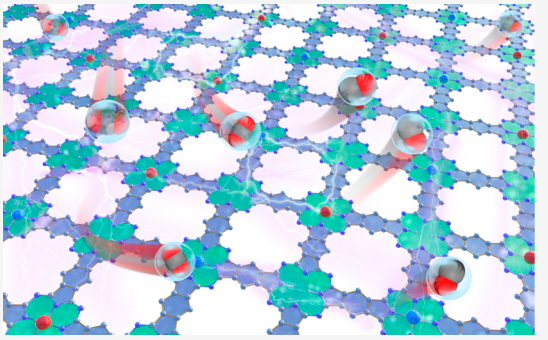

INTRODUCTION

A grand challenge in the development of electrocatalysts lies in the fact that a single catalytic system can seldom control the interplay between activity, selectivity, and stability.[1−3] Homogeneous catalysts typically can be easily functionalized to target activity or selectivity but are prone to deactivation and show a low electron transfer efficiency. While heterogeneous materials usually offer good stability and catalytic activity, the regulation of their performance at the atomic level remains a formidable challenge.[4−7] As an emerging type of candidate for electrocatalysts, reticular materials, including covalent organic frameworks (COFs) and metal−organic frameworks (MOFs), have exhibited great potential for regulating catalysis in a modular and precise way to fill the gap between homogeneous and heterogeneous catalysts.[3,8−10] With the concept of reticular chemistry, desired structures and properties can merge through the self-assembly of extremely simple building elements into solid-state materials with atomically precise structures.[11−14]

Despite the significant progress, there remains an absence of a consummate solution that combines the advantageous properties of homo- and heterogeneous electrocatalysts in a single reticular system. On one hand, although a few successful reticular systems have been developed with good chemical stabilities,[15−19] classical reticular materials, such as MOFs based on carboxylates and COFs based on Schiff base and borate chemistry, often have limited chemical stability, which hampers their practical and long-term use in electrocatalytic conditions.[8,9,20] On the other hand, the choice of building blocks and the way they connect in typical reticular materials usually cannot provide feasible charge transfer, which frequently causes low current density in electrocatalysis.[21,22] More importantly, although the modular construction of reticular materials theoretically allows the installation of various chemical and structural features to modulate the activity and selectivity, such modulations, in most cases, only target one of the performance parameters, with the others marginally improved.[3,22,23] For example, the optimizations of the activity are frequently accompanied by low selectivity and/or stability of the catalysts.[23,24] There is still an urgent need for a type of reticular material platform that integrates crystallinity, stability, conductivity, and tunability for achieving an overall modulation of performance parameters.

We envision that constructing reticular materials featuring fully conjugated skeletons embedded with programmable active sites could be an effective way to integrate the desired features for electrocatalysis into a single system. The molecular structural units connected by fully aromatic linkages will provide rigid scaffolds to ensure high stability and effective

Received: August 8, 2023
Revised: October 11, 2023
Accepted: October 12, 2023
Published: October 27, 2023

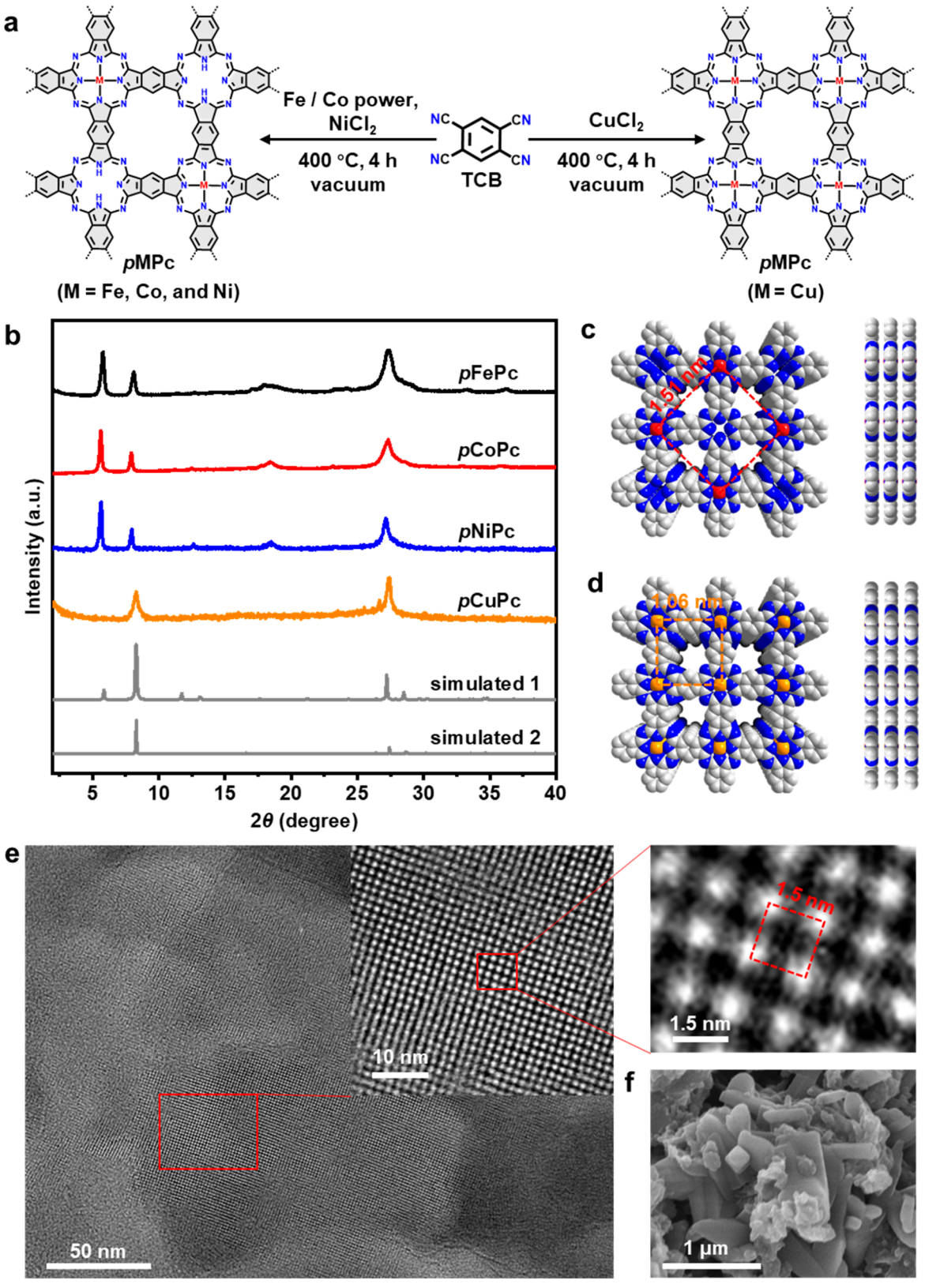

Figure 1. Structure and characterization of *p*MPcs. (a) Schematic representation for the synthesis of *p*MPcs (M = Fe, Co, and Ni) and *p*CuPc with solid-state reactions. (b) Experimental PXRD of *p*MPcs (M = Fe, Co, Ni, and Cu) and simulated PXRD from models in CMMM and P4/MMM space groups, respectively (from top to bottom). Top and side views of a graphical representation of (c) *p*MPcs (M = Fe, Co, and Ni) and (d) *p*CuPc with eclipsed stacking (C, light gray; N, blue; M, red; Cu, orange). (e) TEM (inset of e: locally enlarged TEM image) and (f) SEM images of *p*NiPc.

https://doi.org/10.1021/jacs.3c08594
J. Am. Chem. Soc. 2023, 145, 24230−24239

charge delocalization, for good bulk electrical conductivity.[25−30] Furthermore, in a fully conjugated structure, the electronic communications of the highly delocalized electrons will allow the electronic characteristics of the active sites to be effectively perturbed, resulting in a unique electronic effect.[31]

Herein, we report the synthesis of a family of all aromatically conjugated COFs, polymetallophthalocyanines (*p*MPcs, M = Fe, Co, Ni, and Cu), via the quadruple intermolecular nucleophilic annulation of 1,2,4,5-tetracyanobenzene (TCB) (Figure 1a). The optimized solid-state reaction of TCB results in *p*MPcs with high crystallinity, enabling a new and convincing structural interpretation of *p*MPcs, which was previously elusive. The *p*MPcs exhibit unique electronic properties with good electrical conductivities at the level of 10^{-3}−10^{-1} S m^{-1} and excellent chemical and thermal stability and can serve as a unique and tunable platform in electrochemical catalysis. Especially, due to the aromatically conjugated skeleton, unprecedented long-range interactions between adjacent metal sites can occur to alter the electronic state of active sites. This feature has allowed the construction and utilization of heterobimetallic *p*CoNiPc with a Ni and Co dual-site that can combine the respective advantageous features of *p*NiPc and *p*CoPc in CO_2 reduction to afford a high FE_{CO} of 94%, a high current density of −16.0 mA cm^{-2}, and enhanced long-term stability, making it one of the best-performing CO_2 reduction electrocatalysts among all phthalocyanine- and porphyrin-based materials, as well as in reticular materials.[22,32−36]

RESULTS AND DISCUSSION

Design and Synthesis of *p*MPcs. Metallophthalocyanines have been widely studied as electrocatalysts for their unique chemical and electronic properties.[37,38] *p*MPcs, in which the neighboring metallophthalocyanine units are fused through aromatic rings, have been an interest since the 1950s because of their perfectly ordered network topology and fully aromatically conjugated structures.[39,40] However, their construction is still limited to on-surface synthesis,[31] and the bulk synthesis of high-crystalline *p*MPcs remains a long-lasting challenge.[41,42] Previously, the cyclization reaction of TCB with transition metals at temperatures of 160−350 °C in open containers only leads to amorphous polymeric metallophthalocyanines.[39−41] Considering that those temperatures can be higher than the melting point of TCB (268 °C), which may lead to the ratio of TCB and transition metals deviating from desired stoichiometry due to the loss of TCB at high temperatures, we performed the reaction between TCB and the transition metals using confined containers of sealed Pyrex tubes (inner diameter of 8 mm and length of ca. 5.0 cm) under a vacuum environment at 400 °C for 4 h (Figures S1 and S2). We also noticed that the actual crystallinity of the product depends heavily on the metal source; therefore, metal salts or metallic powders were tested for optimal outcomes (Figure S3). Under our optimized conditions, the polymeric tetracyclization of TCB gave *p*MPcs as a dark green to purple-black powder after purification.

The successful synthesis of highly crystalline *p*MPcs (M = Fe, Co, Ni, and Cu) is first supported by powder X-ray diffraction (PXRD). The PXRD spectra of *p*FePc, *p*CoPc, and *p*NiPc show similar patterns with three strong diffraction peaks at 2θ = 5.64°, 7.98°, and 27.12° (Figures 1b and S4), which are ascribed to planes (100), (010), and (001), respectively. The sharp (100) and (010) diffractions indicate good long-range in-plane periodicity in the three *p*MPcs. Different from these three *p*MPcs (M = Fe, Co, and Ni), in the PXRD profile of *p*CuPc, the diffraction peak at $2\theta \sim 5.6°$ is absent. Instead, two diffractions at 2θ = 8.25° and 27.41° are observed. This difference indicates that *p*CuPc may have a different in-plane periodicity from that of *p*FePc, *p*CoPc, and *p*NiPc. The simulation using models in the CMMM space group with eclipsed cofacial AA-stacking, in which MPc and Pc subunits are alternatively fused in each cofacially stacked layer (Figure 1c), matches the experimental PXRD of *p*FePc, *p*CoPc, and *p*NiPc, while a model in the P4/MMM space group with CuPc units consecutively fused (Figure 1d) gives the best fit for the experimental PXRD of *p*CuPc. Powder refinement of the experimental PXRD reaches good consistency with residual values of less than 5% for all of the *p*MPcs, further validating the above structural analysis (Figures S5−S8).

Inductively coupled plasma atomic emission spectrometer (ICP-AES) results show that the metal content is 6.44%, 6.70%, and 7.31% for *p*FePc, *p*CoPc, and *p*NiPc, respectively, which matches reasonably to their corresponding theoretical values of 7.27%, 7.64%, and 7.61% based on the above models. Differently, the copper content in *p*CuPc was found to be 13.26%, nearly double that for *p*MPc (M = Fe, Co, and Ni) and compliant with the model with a theoretical Cu content of 15.14% (Tables S1−S4). Scanning electron microscopy (SEM) images show nanometer-sized grains with irregular to rectangular grains in the samples of *p*MPc (Figures 1f and S9−S11). Transmission electron microscopy (TEM) observations for *p*MPcs (M = Fe, Co, and Ni) show regular lines with a spacing of 1.5 nm. Prominently, a square lattice with a side length of 1.5 nm can be observed in the TEM image of *p*NiPc. This feature matches exactly with the square grid structure (theoretical side length of 1.51 nm) of *p*MPcs (M = Fe, Co, and Ni) that consists of the MPc and Pc fragment (Figures 1e, S12, and S13). The N_2 sorption isotherms measured at 77 K show that the Brunauer−Emmett−Teller (BET) surface areas of *p*MPcs are 205, 176, 258, and 295 m^2 g^{-1} for *p*FePc, *p*CoPc, *p*NiPc, *p*NiPc, and *p*CuPc, respectively. The pore size distribution indicates that *p*MPcs have a microporous structure (Figure S14). Meanwhile, analysis of CO_2 adsorption isotherms reveals that the heat of CO_2 adsorption of *p*MPcs is in the range of 30−42 kJ mol^{-1}, indicating their good CO_2 affinity (Figures S15 and S16 and Table S5).

The above results point to a conclusion that *p*MPcs have two types of configurations depending on the identity of the central metal, in which *p*FePc, *p*CoPc, and *p*NiPc are composed of alternatively fused MPc and Pc subunits, while *p*CuPc is fused solely with the CuPc subunit. The structural insight we provide is in stark comparison with the previous understanding of the structures for *p*MPcs where fused structures of solely MPc units had been proposed.[40,41] Fourier transform infrared (FT-IR) spectroscopy further supports the formation of *p*MPcs (Figures S17 and S18).[6]

Stabilities of *p*MPcs. Thermogravimetric analysis of *p*MPcs exhibits a weight loss < 10% in a N_2 atmosphere at temperatures of up to 450 °C (Figures S19−S22), indicating their good thermal stabilities. After being treated with extremely acidic and basic conditions in 6 M H_2SO_4 and KOH for 1 week, the crystallinities of *p*MPcs are well maintained (Figures S23−S26), demonstrating their excellent resistance to harsh chemical stress attributed to their aromatically conjugated skeleton.

https://doi.org/10.1021/jacs.3c08594
J. Am. Chem. Soc. 2023, 145, 24230−24239

Electronic Properties of *p*MPcs. The K-edge extended X-ray absorption fine structure (EXAFS) curves of the metal in *p*MPcs show a dominant peak at ~1.4 Å ascribed to the metal−N scattering path, which is nearly the same as in molecular MPcs, consistent with the analysis of X-ray absorption near-edge structure (XANES) spectra (Figures 2a,c and S27−S32). X-ray photoelectron spectroscopy (XPS)

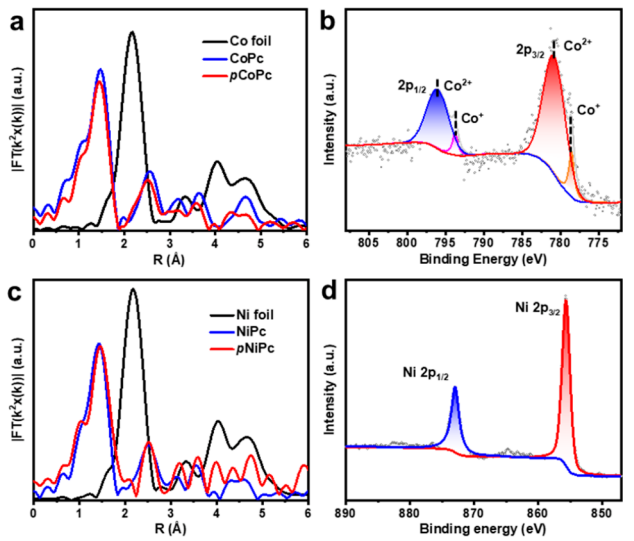

Figure 2. Electronic properties of *p*CoPc and *p*NiPc. The K-edge EXAFS spectra of (a) *p*CoPc, CoPc, and Co foil and (c) *p*NiPc, NiPc, and Ni foil. High-resolution (b) Co 2p XPS spectrum of *p*CoPc and (d) Ni 2p XPS spectrum of *p*NiPc.

indicates the coexistence of Fe^{2+}/Fe^{3+} in *p*FePc (Figure S33). The Co in *p*CoPc and Cu in *p*CuPc present a mixed valence of +1/+2 with Co^{2+} and Cu^{2+} as the dominant species (Figures 2b and S34). In *p*NiPc, the metals exist exclusively as the +2 state (Figure 2d), consistent with their electron paramagnetic resonance (EPR) spectra where ligand- and metal-centered signals are expected to be present (Figures S35−S38), respectively.

The conductivities of bulk *p*FePc, *p*CoPc, *p*NiPc, and *p*CuPc measured at 298 K by the four probe method after cold pressing are 1.49×10^{-1}, 4.88×10^{-3}, 4.02×10^{-3}, and 1.82×10^{-3} S m^{-1}, respectively (Table S6). Compared with molecular MPc analogs with typical conductivities in the range of 10^{-9}−10^{-12} S m^{-1}, *p*MPcs have 7−9 orders of magnitude improved conductivities.[41,43,44] These prominent improvements are likely due to the formation of the extended aromatically conjugated planes in *p*MPcs,[36,45] as evidenced by the much wider and red-shifted ultraviolet−visible−near-infrared spectra (Figures S39−S42). The conductivities of *p*MPcs are among the highest in the covalently linked reticular materials[22,27] and are even comparable to some MPc-containing conjugated MOFs.[23] Band structure and density of states calculations indicated that both the in-plane charge transport from their large π-conjugation and out-of-plane charge transport due to the formation of periodic π-columns contribute to the good conductivities (Figures S43−S46). We notice that the features of band structure of *p*MPcs are consistent with those of other phthalocyanine- and porphyrin-based 2D reticular materials, indicating that the high conductivity found in *p*MPcs likely is rooted in their π-conjugated and stacked structures, like those in the reported examples.[23,27,30]

Electrocatalytic CO_2RR Performance of *p*MPcs. We propose that *p*MPcs with the metal sites uniformly dispersed in fully aromatically conjugated and stable scaffolds will serve as truly appealing electrochemical catalysts. Consequently, we assessed the activity and selectivity of *p*MPcs for the electrocatalytic CO_2 reduction reaction (CO_2RR). For a parallel comparison, we choose the electrolyte with a pH of 7.2 and a catalyst loading of 1.0 mg cm^{-2} for our study (Figure S47). The CO_2 reduction products are dominated by CO and H_2 (Figure S48). The four *p*MPcs exhibit metal identity-dependent CO_2RR performance, in which *p*CoPc and *p*NiPc stand out regarding the activity and selectivity (Figure 3a and

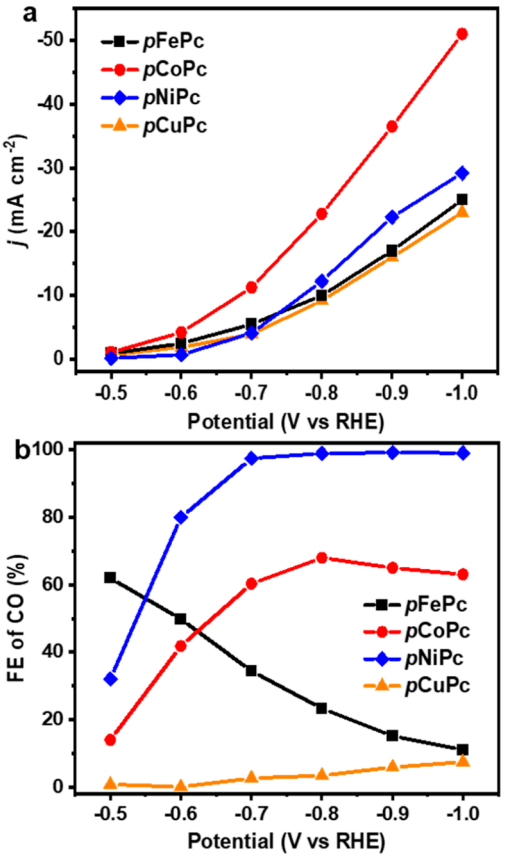

Figure 3. Electrochemical performances for CO_2 reduction over *p*MPcs. (a) Current density of *p*MPcs under different potentials in 0.5 M $KHCO_3$. (b) FE_{CO} values of *p*MPcs under different potentials.

b). Double-layer capacitance (C_{dl}) values of *p*CoPc and *p*NiPc are calculated to be 57.12 and 62.73 mF/cm^2, respectively, indicating their abundant catalytic sites (Figure S49). Among *p*MPcs, *p*NiPc has the highest CO selectivity with a FE_{CO} of 99% and high activity with a current density (j) of −12.2 mA cm^{-2} at −0.8 V (vs RHE). *p*CoPc exhibits a moderately high CO selectivity with a FE_{CO} of 67% and the highest activity with a j of up to −22.8 mA cm^{-2}. Electrochemical impedance (−0.8 V vs RHE) and Tafel slope both give consistent trends with the observed activity in the CO_2RR test (Figures S50 and S51). The current densities obtained by all four *p*MPcs are much higher than those of molecular MPcs at most of the tested potentials (Figure S52). The superior activity of *p*MPcs over molecular MPcs may be ascribed to the good conductivities of *p*MPcs that facilitate charge transport involved in the electrochemical reduction of CO_2.[23,44]

https://doi.org/10.1021/jacs.3c08594
J. Am. Chem. Soc. 2023, 145, 24230−24239

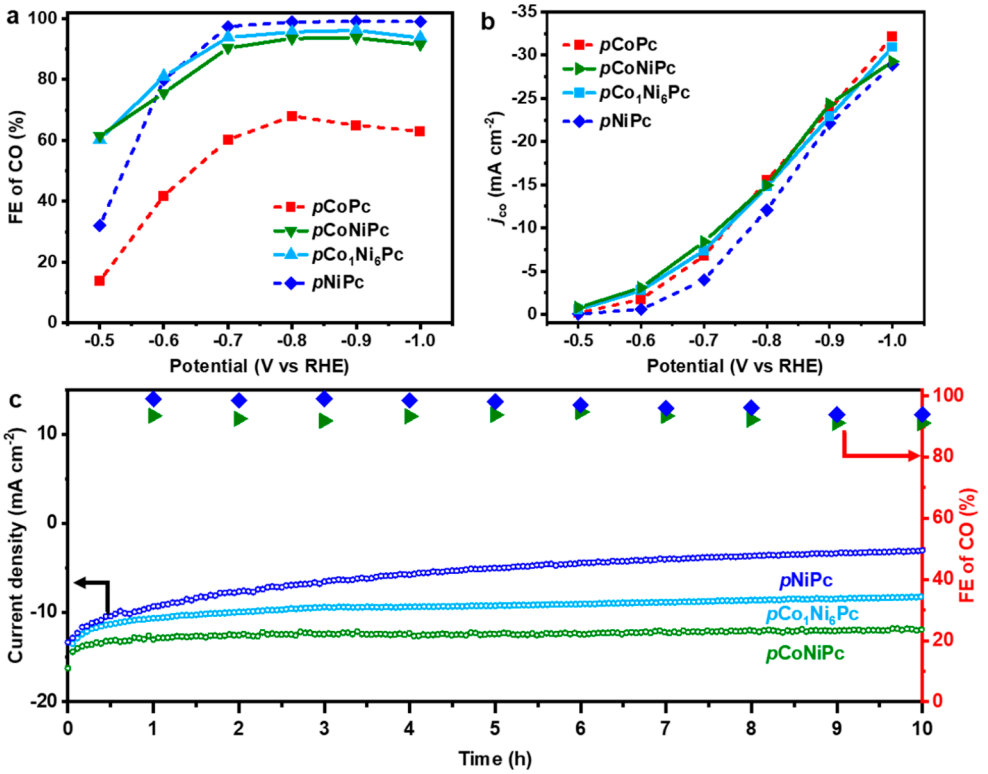

Figure 4. Electrochemical CO_2RR performance comparison plots of heterobimetallic *p*MPcs and *p*MPcs. (a) FE_{CO} and (b) j_{CO} for *p*CoPc, *p*CoNiPc, *p*Co_1Ni_6Pc, and *p*NiPc under different potentials in 0.5 M $KHCO_3$. (c) Stability test of *p*CoNiPc, *p*Co_1Ni_6Pc, and *p*NiPc at −0.8 V (vs RHE).

Stability, another crucial electrocatalyst evaluation criterion, was assessed for electrocatalytic CO_2RR over an extended period under a fixed potential. The *p*NiPc shows a noticeable decay in the current density and a slightly decreasing FE_{CO} (Figure S53). In contrast, *p*CoPc displays excellent stability during continuous electrolysis regarding the current density and FE_{CO} (Figure S54). The slow degradation of the activity and selectivity with time in *p*NiPc while absent in *p*CoPc may be due to reduction-caused metal leaching at high reduction potential.[46] This discriminated electrolytic stability has been observed in other MPc-based composite materials, in which the high reduction potential can lead to the deformation of the NiN_4 configuration and subsequent demetalation.[46,47] XRD, SEM, and TEM characterizations of *p*CoPc and *p*NiPc show that their crystallinity and morphology are maintained after electrolysis (Figures S55−S57). The Co content of *p*CoPc is maintained, while the Ni content of *p*NiPc has been found with a slight decrease (Table S7), which may be correlated to their different stabilities in the long-time electrolysis.

Electrocatalytic CO_2RR Using Hetero-Bimetallic *p*MPcs. Given the encouraging outcome that *p*NiPc offers excellent CO selectivity and *p*CoPc gives excellent activity and stability, we further aim to integrate those advantageous catalytic features of *p*NiPc and *p*CoPc through the construction of a dual-site catalyst by taking advantage of the modular availability of *p*MPcs.[48] The simultaneous presence of two active metal centers can lead to emergent catalytic performance through the occurrence of specific electronic interactions between the combined active sites.[49−54] Toward this end, we have synthesized dual-site *p*MPcs with Co and Ni in molar ratios close to 1:1 and 1:6, named *p*CoNiPc and *p*Co_1Ni_6Pc, respectively, which are both crystalline and share an isoreticular structure with *p*MPcs (M = Fe, Co, and Ni) (Figures S14, S15, and S58−S64 and Tables S5 and S8).

Notably, both *p*CoNiPc and *p*Co_1Ni_6Pc exhibited high selectivities with FE_{CO} > 90% at the potential range of −0.7 to −1.0 V (Figure 4a), which are more than 50% improvements compared to those of *p*CoPc and are close to those of *p*NiPc under the same conditions. With the increase in Ni content from *p*CoNiPc to *p*NiPc, the CO selectivity is slightly increased. The current densities of *p*CoNiPc and *p*Co_1Ni_6Pc, especially at the range of −0.6 to −0.9 V, also exhibit prominent improvements compared with that of *p*NiPc (Figure 4b). At −0.8 V, the partial current density j_{CO} of *p*CoNiPc reaches −15.0 mA cm^{-2}, 25% higher than that of *p*NiPc and rather close to that of *p*CoPc. Moreover, the long-time electrolysis test shows that utilization of the dual-site can significantly enhance the stability of the catalysts (Figure 4c). The enhancement seems to be associated with the ratio of Co/Ni, as a more remarkable reinforcement of stability has been observed for *p*CoNiPc than *p*Co_1Ni_6Pc. The current density and Faradaic efficiency for *p*CoNiPc both show negligible changes during the 10 h electrolysis test. Characterizations using PXRD, FT-IR, SEM, and TEM results show that the structure and morphology can be preserved after electrocatalysis (Figures S57 and S65−S67), as well as the content and valence state of Ni and Co in *p*CoNiPc as verified by XPS and ICP-AES (Figure S68 and Table S7).

Using a flow cell setup that can circumvent the transport limitation of CO_2, the current density of *p*CoNiPc reaches an industrially relevant level of −100 mA cm^{-2} at −0.8 V, six times that in the H-type cell (Figure S69). The *p*CoNiPc can maintain nearly 100% of its initial current density and FE_{CO} during 10 h of continuous operation, manifesting its out-

https://doi.org/10.1021/jacs.3c08594
J. Am. Chem. Soc. 2023, 145, 24230−24239

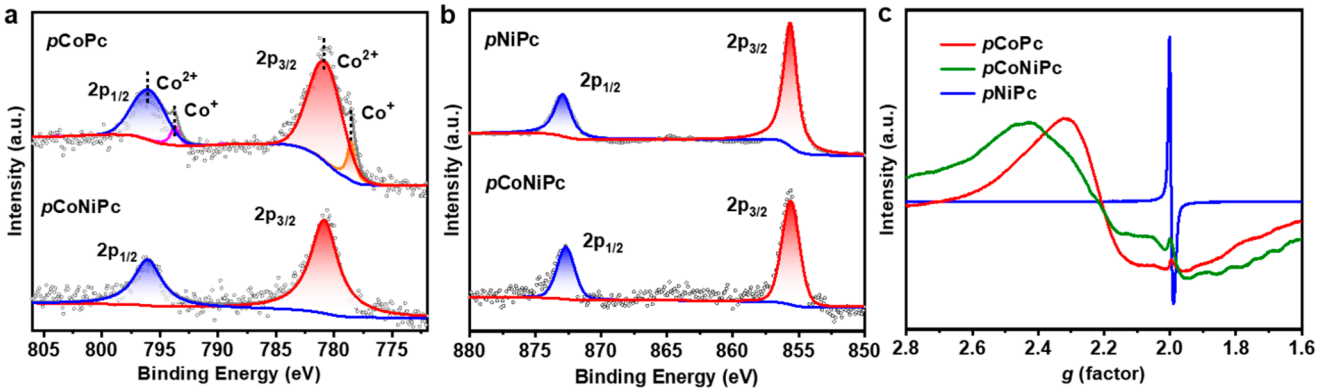

Figure 5. Comparison of electronic properties between *p*CoNiPc and *p*MPcs. High-resolution XPS (a) Co 2p spectra of *p*CoPc and *p*CoNiPc-Co and (b) Ni 2p spectra of *p*NiPc and *p*CoNiPc-Ni. (c) EPR spectra of *p*NiPc, *p*CoPc, and *p*CoNiPc.

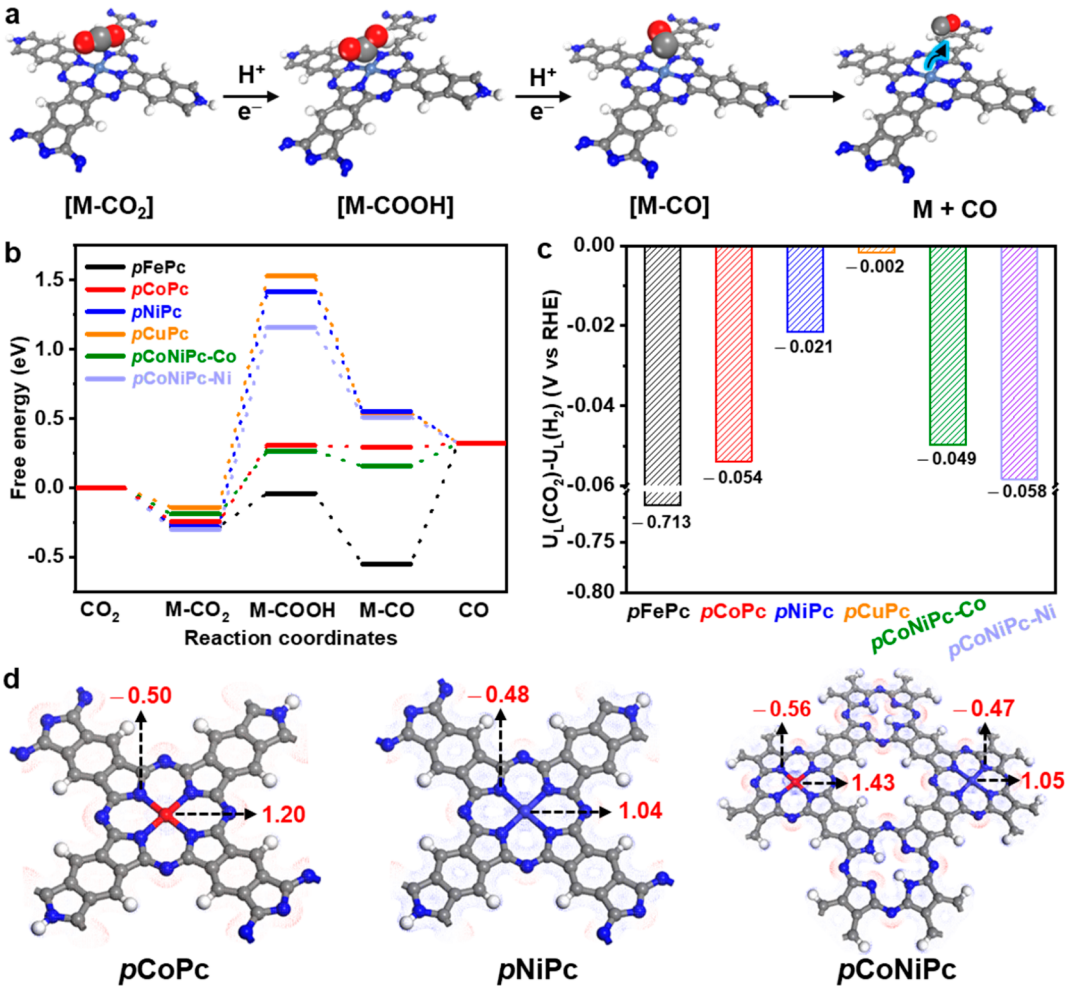

Figure 6. Computational results of CO_2 reduction over *p*MPcs. (a) Reaction pathway and (b) free energy diagrams of the reduction of CO_2 to CO. (c) The values of $U_L(CO_2) - U_L(H_2)$ for *p*MPcs catalysts. (d) Mulliken charge analysis of the metal sites and the surrounding N atoms and electrostatic potential diagram for *p*CoPc, *p*NiPc, and *p*CoNiPc (isovalue 0.3 eV).

standing long-term stability under industrially relevant conditions. $^{13}CO_2$ isotope experiments of *p*CoNiPc at these conditions demonstrate that CO_2 is the exclusive source of product CO (Figure S70). The above results unambiguously demonstrate that the combination of Co and Ni sites in the aromatically conjugated scaffolds has achieved superior selectivity, activity, and stability with a single reticular electrocatalyst.

Mechanistic Study of Hetero-Bimetallic *p*MPcs for CO_2RR. To explore the underlying mechanism responsible for the observed CO_2RR performance of *p*MPcs, a series of experimental and theoretical studies have been performed. The XPS spectra show that compared to single-site *p*MPcs, the Co 2p spectrum of *p*CoNiPc only shows peaks ascribed to Co^{2+} (Figure 5a), and the spectrum of Ni 2p shows negligible changes (Figure 5b), suggesting that the electronic state of the

https://doi.org/10.1021/jacs.3c08594
J. Am. Chem. Soc. 2023, 145, 24230−24239

Co site in *p*CoNiPc becomes more positive from a mixed +1/+2 state to a pure +2 state, while the state of the Ni site is barely shifted. The peak ascribed to the Co-centered radical in the EPR spectrum of *p*CoNiPc shows a prominent low-field shift and broadening compared to that of *p*CoPc (Figure 5c), which is a sign of enhanced charge transfer between Co and the Pc ligand.[55,56]

DFT calculations suggest that the formation of M-COOH is the rate-determining step (RDS) for single-site and dual-site *p*MPcs except for *p*FePc, for which the desorption of CO is the RDS (Figure 6a and Tables S9−S14).[23,57,58] The calculated activation free energy (ΔG) of CO production is 0.87, 0.55, 1.68, and 1.67 eV for *p*FePc, *p*CoPc, *p*NiPc, and *p*CuPc, respectively (Figure 6b). The lowest ΔG of *p*CoPc suggests its highest activity among all of the single-site *p*MPcs. After the incorporation of Co and Ni in *p*CoNiPc, an activation energy of 0.46 eV, close to that in *p*CoPc, is observed when CO_2 reduction occurs on the Co site of *p*CoNiPc. This observation agrees well with the comparable activity between *p*CoNiPc and *p*CoPc. The comparison of activation energy indicates that Co is the more favored active site over Ni in *p*CoNiPc.

The limiting potential difference between the CO_2RR and hydrogen evolution reaction ($U_L(CO_2) - U_L(H_2)$, $U_L = -\Delta G/e$) has been calculated and used as a descriptor for evaluating CO selectivity. A more positive value of $U_L(CO_2) - U_L(H_2)$ corresponds to a higher selectivity of CO_2RR.[50,58,59] As shown in Figure 6c, the $U_L(CO_2) - U_L(H_2)$ values of *p*FePc, *p*CoPc, and *p*NiPc are −0.713, −0.054, and −0.021, respectively, indicating a CO selectivity order of *p*NiPc > *p*CoPc > *p*FePc (Figure S71). Moreover, the $U_L(CO_2) - U_L(H_2)$ value of *p*CoNiPc with Co as the active site is more positive than that of *p*CoPc but is more negative than that of *p*NiPc. Thus, the comparison of $U_L(CO_2) - U_L(H_2)$ values suggests a CO selectivity trend of *p*NiPc > *p*CoNiPc > *p*CoPc, in agreement with the experimental results. Calculations using a double-layer model yield consistent results for *p*CoPc, *p*NiPc, and *p*CoNiPc (Figures S72−74). The discrepancy between the calculated results and experimental observations for *p*CuPc may be due to the lack of consideration of electrolyte and the state of the catalyst (e.g., the morphology, availability of the active sites, and the presence of defects) in the calculation.[60]

The calculated Mulliken charge density of the Co site in *p*CoNiPc is 1.43, much higher than 1.20 for the Co site in *p*CoPc (Figure 6d). The charge densities of the Ni sites in *p*NiPc and *p*CoNiPc are quite similar, which are 1.04 and 1.05, respectively. Interestingly, the Mulliken charge densities of the four N atoms surrounding the Co site in *p*CoNiPc are more negative than those in *p*CoPc (−0.56 vs −0.50), respectively. These values suggest that the existence of Ni sites induces charge redistribution between the Co site and the Pc ligand of *p*CoNiPc, in which the presence of Ni sites leads to a net electron transfer from the Co site to its adjacent N atoms. These computational insights, along with the observation by XPS and EPR, evidence the electron transfer from Co to the N atoms, which supports effective interactions between the embedded Co and Ni sites in *p*CoNiPc.[52] Compared with *p*CoPc, the higher positive charge density and more positive electrostatic potential of the Co sites in *p*CoNiPc will make it more conducive for stabilizing COOH to improve the activity and selectivity.

In typical diatomic site catalyst systems, a close atomic distance is required to allow orbital coupling to initiate internal electronic interactions, so as to profoundly vary the electronic properties of heteroatoms. It is generally believed that when the distance between the two atoms is larger than 4−15 Å, they are thought to be unrelated.[52] It is worth noting that, in our case, it is the long-range interactions that play a role,[52] because the distance between Co and Ni in diatomic *p*MPcs, for instance, *p*CoNiPc, is 1.5 nm or larger based on the model for *p*MPcs (M = Fe, Co, and Ni). Such a long-range interaction takes effect over a large interatomic separation across 14 chemical bonds (Figure S75), which, to our knowledge, has never been previously observed.

CONCLUSIONS

We have synthesized a new class of conductive COFs, named *p*MPcs, through solid-phase synthesis, which provides a facile and robust approach to crystalline polymeric metallophthalocyanines with well-defined aromatically conjugated structures that has been challenging for decades. The access to *p*MPcs opens the door for the development of electrocatalysts with precisely distributed single and multiple sites that are based on crystalline, conductive, and stable reticular materials. The highly crystalline nature and modular synthesis of *p*MPcs ensure a solid interpretation of the catalytic performance, while producing tunability of performance building upon the electrocatalytic results from single-site *p*MPcs. The construction of bimetallic *p*CoNiPc realizes the marriage of remarkable selectivity, activity, and stability for the CO_2RR into a single system, which can compete with the state-of-the-art reticular materials and composite materials made of MPc or metalloporphyrin with carbon nanotubes for the CO_2RR (Table S15). Harnessing the tunability resulting from the long-range interactions of the embedded sites in *p*MPcs, the combination of other metal sites with distinct catalytic features should emerge with more demanded catalytic behavior that will find applications far beyond CO_2RR.

MATERIALS AND METHODS

Materials and Characterizations. All chemicals were purchased without further treatment. PXRD patterns were collected on a Japan Rigaku MiniFlex 600 equipped with graphite-monochromatized Cu Kα radiation (λ = 1.541 Å). Nitrogen sorption analysis was carried out at 77 K using the Micromeritics ASAP 2020 automatic volumetric adsorption system. The microstructure and morphology of the material were observed by a Carl Zeiss Supra 40 SEM. TEM images were obtained on a JEM-2010F. The high-angle annular dark-field scanning transmission electron microscopy (HAADF-STEM) and energy dispersive spectroscopy (EDS) mapping analyses were performed on a Talos F200X instrument equipped with Super-X EDX operating at 200 kV. Thermogravimetric analysis (TGA) was conducted on a TGA Q5000 integrated thermal analyzer at a heating rate of 5 °C min^{-1} under a N_2 atmosphere. UV−vis−IR spectra of the catalysts were collected on a Shimadzu UV-3600 Plus. FT-IR spectra were obtained using a Bruker Tensor II FT-IR spectrometer with KBr pellets at 400−4000 cm^{-1}. EPR signals were collected on a JEOL JES-FA200 EPR spectrometer at room temperature. XPS experiments were conducted on an ESCALAB 250 high-performance electron spectrometer using the excitation source of monochromatized Al Kα ($h\nu$ = 1486.7 eV). Elemental (C, H, and N) analysis was performed by a VarioELIII German Elemental Analysis Systems Inc. using the combustion method by automatic analyzers. The contents of metal (Fe, Co, Ni, and Cu) were estimated by using an Optima 7300 DV inductively coupled plasma atomic emission spectrometer. The liquid products were examined by nuclear magnetic resonance (NMR) (Bruker AVANCE AV III 400) spectroscopy.

Synthesis of *p*MPcs (M = Fe, Co, Ni, and Cu), *p*Co_1Ni_6Pc, and *p*CoNiPc. For the synthesis of *p*MPcs (M = Fe, Co, Ni, and Cu), TCB (50 mg, 0.28 mmol) was mixed with iron powder (31.5 mg, 0.56

https://doi.org/10.1021/jacs.3c08594
J. Am. Chem. Soc. 2023, 145, 24230−24239

mmol), cobalt powder (33 mg, 0.56 mmol), anhydrous nickel chloride (72.5 mg, 0.56 mmol), and anhydrous copper chloride (38 mg, 0.28 mmol), respectively. The mixture was thoroughly ground and transferred into a Pyrex tube measuring o.d. × i.d. = 10 × 8 mm^2. The Pyrex tube was then evacuated and flame-sealed with the total length kept at ca. 5.0 cm. The glass tube was heated to 400 °C at 5 °C/min and kept for 4 h in a tube furnace under vacuum conditions. After cooling to room temperature, the product was washed several times with ethanol, iron chloride solution, and H_2O and then dried at 60 °C in a vacuum oven to afford a purple-black powder. *p*Co_1Ni_6Pc and *p*CoNiPc were synthesized using the same procedure except that TCB was mixed with cobalt powder and anhydrous nickel chloride in molar ratios of 1:1:1 and 1:0.75:0.25, respectively.

Stability Test. Ten milligrams of each *p*MPc sample was soaked and stirred in aqueous H_2SO_4 (6 M) and KOH (6 M) solutions, respectively, at room temperature for 1 week. Before PXRD measurements, the treated *p*MPcs samples were successively washed with water (8 mL × 5) and ethanol (8 mL × 2) and then dried at 60 °C under vacuum overnight.

X-ray Absorption Spectra. The X-ray absorption fine structure (XAFS) spectra for the K-edge absorption of Fe, Co, Ni, and Cu were collected at beamline 1W1B of the Beijing Synchrotron Radiation Facility.

EPR Measurements. EPR spectra were collected on a JEOL JES-FA200 EPR spectrometer. EPR spectra of solid powder were measured at room temperature in air by taking 2 mg of the sample and placing it into an EPR tube.

Conductivity Measurement. To make a pressed pellet, ~40 mg of the sample was put into an 8 mm inner-diameter split sleeve pressing die and pressed for 5 min under a pressure of approximately 600 psi. A Singatone tungsten carbide four-point linear probe was employed to collect bulk conductivity measurements of the *p*MPcs.

Electrochemical Measurements. Electrochemical measurements were conducted with a CHI 760E electrochemical analyzer (CH Instruments, Inc., Shanghai). The electrolyzer for CO_2 electrochemical reduction was an H-type cell separated by a cation exchange membrane (Nafion115, Dupont). All potentials reported in this work were converted from vs Ag/AgCl to vs RHE by adding a value of 0.197 + 0.059 × pH. According to the literature, the pH of 0.5 M $KHCO_3$ saturated with pure CO_2 is 7.2.[61]

The FE efficiencies of CO and H_2 are calculated according to the following formula:

$$\mathrm{FE} = \frac{j}{j_{\mathrm{total}}} = \frac{nNF}{j_{\mathrm{total}}} \tag{1}$$

in which FE is the faradaic efficiency of CO or H_2, j is the partial current density of CO or H_2 production, j_{total} is the total current density, n is the production rate of CO or H_2, N is electron transfer number, which is 2 for CO and H_2, and F is faradaic constant (96485 C/mol).

The Tafel slope was calculated using the following formula:

$$\eta = b \log\left(\frac{j_{\mathrm{total}}}{j_{co}}\right) \tag{2}$$

where η is the CO_2RR overpotential (mV), b is the Tafel slope (mV dec^{-1}), and j_{total} and j_{CO} are respectively the total current density and partial current density for CO (mA cm^{-2}).

Computational Details. Electronic calculations were performed to optimize the geometry and calculate the Gibbs free energy of all intermediates involved in the reactions using density functional theory (DFT) in the Dmol3 module of Materials Studio (Figure S76). Equations 3 and 4 are used to calculate the free energy for each adsorbed and gas-phase species.

$$G = H - TS = E_{\mathrm{DFT}} + E_{\mathrm{ZPE}} + \int_0^{298.15} C_p \, \mathrm{d}T - TS \tag{3}$$

$$\mu(\mathrm{H}^+) + \mu(\mathrm{e}^-) = 1/2\mu[\mathrm{H}_2(\mathrm{g})] \tag{4}$$

In eq 3, T is the system temperature (298.15 K), E_{DFT} is the electron energy calculated by DFT above, E_{ZPE} is the zero-point energy, which is a combination of vibrational, translational, and rotational energy at absolute zero, C_p is the heat capacity, and S is entropy. E_{ZPE}, C_p, and S are calculated using the harmonic approximation of the frequency analysis in the Dmol3 module.[62]

■ ASSOCIATED CONTENT

Supporting Information

The Supporting Information is available free of charge at https://pubs.acs.org/doi/10.1021/jacs.3c08594.

Details on linker preparation, characterization data, and figures (PDF)

■ AUTHOR INFORMATION

Corresponding Authors

Zheng Meng − *Hefei National Research Center for Physical Sciences at the Microscale, Department of Chemistry, University of Science and Technology of China, Hefei, Anhui 230026, People's Republic of China*; Email: zhengmeng@ustc.edu.cn

Hai-Long Jiang − *Hefei National Research Center for Physical Sciences at the Microscale, Department of Chemistry, University of Science and Technology of China, Hefei, Anhui 230026, People's Republic of China; Institute of Energy, Hefei Comprehensive National Science Center, Hefei, Anhui 230031, People's Republic of China*; orcid.org/0000-0002-2975-7977; Email: jianglab@ustc.edu.cn

Authors

Yi Zhang − *Hefei National Research Center for Physical Sciences at the Microscale, Department of Chemistry, University of Science and Technology of China, Hefei, Anhui 230026, People's Republic of China*

Xiyuan Zhang − *Hefei National Research Center for Physical Sciences at the Microscale, Department of Chemistry, University of Science and Technology of China, Hefei, Anhui 230026, People's Republic of China*

Long Jiao − *Hefei National Research Center for Physical Sciences at the Microscale, Department of Chemistry, University of Science and Technology of China, Hefei, Anhui 230026, People's Republic of China; Institute of Energy, Hefei Comprehensive National Science Center, Hefei, Anhui 230031, People's Republic of China*

Complete contact information is available at: https://pubs.acs.org/10.1021/jacs.3c08594

Author Contributions

All authors have given approval to the final version of the manuscript.

Notes

The authors declare no competing financial interest.

■ ACKNOWLEDGMENTS

This work was supported by the National Key Research and Development Program of China (2021YFA1500400), the Strategic Priority Research Program of the Chinese Academy of Sciences (XDB0450302), the National Natural Science Foundation of China (U22A20401 and 22161142001), Major Industrial Innovation Plan of Anhui Province (AHZDCYCX-LSDT2023-04), and the University Synergy Innovation

Program of Anhui Province (GXXT-2022-006). The authors thank the 1W1B station at BSRF for XAFS measurements.

REFERENCES

(1) Aresta, M.; Dibenedetto, A.; Angelini, A. Catalysis for the Valorization of Exhaust Carbon: From CO_2 to Chemicals, Materials, and Fuels. Technological Use of CO_2. *Chem. Rev.* **2014**, *114*, 1709−1742.

(2) Masa, J.; Andronescu, C.; Schuhmann, W. Electrocatalysis as the Nexus for Sustainable Renewable Energy: The Gordian Knot of Activity, Stability, and Selectivity. *Angew. Chem., Int. Ed.* **2020**, *59*, 15298−15312.

(3) Diercks, C. S.; Liu, Y.; Cordova, K. E.; Yaghi, O. M. The Role of Reticular Chemistry in the Design of CO_2 Reduction Catalysts. *Nat. Mater.* **2018**, *17*, 301−307.

(4) Chen, Y.; Li, C. W.; Kanan, M. W. Aqueous CO_2 Reduction at Very Low Overpotential on Oxide-Derived Au Nanoparticles. *J. Am. Chem. Soc.* **2012**, *134*, 19969−19972.

(5) Azaiza-Dabbah, D.; Vogt, C.; Wang, F.; Masip-Sánchez, A.; de Graaf, C.; Poblet, J. M.; Haviv, E.; Neumann, R. Molecular Transition Metal Oxide Electrocatalysts for the Reversible Carbon Dioxide-Carbon Monoxide Transformation. *Angew. Chem., Int. Ed.* **2022**, *61*, No. e202112915.

(6) Han, N.; Wang, Y.; Ma, L.; Wen, J.; Li, J.; Zheng, H.; Nie, K.; Wang, X.; Zhao, F.; Li, Y.; Fan, J.; Zhong, J.; Wu, T.; Miller, D. J.; Lu, J.; Lee, S.-T.; Li, Y. Supported Cobalt Polyphthalocyanine for High-Performance Electrocatalytic CO_2 Reduction. *Chem.* **2017**, *3*, 652−664.

(7) Wang, R.; Wang, X.; Weng, W.; Yao, Y.; Kidkhunthod, P.; Wang, C.; Hou, Y.; Guo, J. Proton/Electron Donors Enhancing Electrocatalytic Activity of Supported Conjugated Microporous Polymers for CO_2 Reduction. *Angew. Chem., Int. Ed.* **2022**, *61*, No. e202115503.

(8) Furukawa, H.; Cordova, K. E.; O'Keeffe, M.; Yaghi, O. M. The Chemistry and Applications of Metal-Organic Frameworks. *Science* **2013**, *341*, 1230444.

(9) Liu, R.; Tan, K.; Gong, Y.; Chen, Y.; Li, Z.; Xie, S.; He, T.; Lu, Z.; Yang, H.; Jiang, D. Covalent Organic Frameworks: an Ideal Platform for Designing Ordered Materials and Advanced Applications. *Chem. Soc. Rev.* **2021**, *50*, 120−242.

(10) Diercks, C. S.; Yaghi, O. M. The Atom, the Molecule, and the Covalent Organic Framework. *Science* **2017**, *355*, eaal1585.

(11) Yaghi, O. M. Reticular Chemistry in All Dimensions. *ACS Cent. Sci.* **2019**, *5*, 1295−1300.

(12) Kuhn, P.; Antonietti, M.; Thomas, A. Porous, Covalent Triazine-Based Frameworks Prepared by Ionothermal Synthesis. *Angew. Chem., Int. Ed.* **2008**, *47*, 3450−3453.

(13) Jackson, K. T.; Reich, T. E.; El-Kaderi, H. M. Targeted Synthesis of a Porous Borazine-Linked Covalent Organic Framework. *Chem. Commun.* **2012**, *48*, 8823−8825.

(14) Côté, A. P.; Benin, A. I.; Ockwig, N. W.; O'Keeffe, M.; Matzger, A. J.; Yaghi, O. M. Porous, Crystalline, Covalent Organic Frameworks. *Science* **2005**, *310*, 1166−1170.

(15) Kandambeth, S.; Mallick, A.; Lukose, B.; Mane, M. V.; Heine, T.; Banerjee, R. Construction of Crystalline 2D Covalent Organic Frameworks with Remarkable Chemical (Acid/Base) Stability via a Combined Reversible and Irreversible Route. *J. Am. Chem. Soc.* **2012**, *134*, 19524−19527.

(16) Jin, E.; Asada, M.; Xu, Q.; Dalapati, S.; Addicoat, M. A.; Brady, M. A.; Xu, H.; Nakamura, T.; Heine, T.; Chen, Q.; Jiang, D. Two-Dimensional sp^2 Carbon-Conjugated Covalent Organic Frameworks. *Science* **2017**, *357*, 673−676.

(17) Guan, X.; Li, H.; Ma, Y.; Xue, M.; Fang, Q.; Yan, Y.; Valtchev, V.; Qiu, S. Chemically Stable Polyarylether-Based Covalent Organic Frameworks. *Nat. Chem.* **2019**, *11*, 587−594.

(18) Férey, G.; Mellot-Draznieks, C.; Serre, C.; Millange, F.; Dutour, J.; Surblé, S.; Margiolaki, I. A Chromium Terephthalate-Based Solid with Unusually Large Pore Volumes and Surface Area. *Science* **2005**, *309*, 2040−2042.

(19) Park, K. S.; Ni, Z.; Côté, A. P.; Choi, J. Y.; Huang, R.; Uribe-Romo, F. J.; Chae, H. K.; O'Keeffe, M.; Yaghi, O. M. Exceptional Chemical and Thermal Stability of Zeolitic Imidazolate Frameworks. *Proc. Natl. Acad. Sci. U.S.A.* **2006**, *103*, 10186−1019.

(20) Ding, M.; Flaig, R. W.; Jiang, H.-L.; Yaghi, O. M. Carbon Capture and Conversion Using Metal-Organic Frameworks and MOF-Based Materials. *Chem. Soc. Rev.* **2019**, *48*, 2783−2828.

(21) Diercks, C. S.; Lin, S.; Kornienko, N.; Kapustin, E. A.; Nichols, E. M.; Zhu, C.; Zhao, Y.; Chang, C. J.; Yaghi, O. M. Reticular Electronic Turning of Porphyrin Active Sites in Covalent Organic Frameworks for Electrocatalytic Carbon Dioxide Reduction. *J. Am. Chem. Soc.* **2018**, *140*, 1116−1122.

(22) Lin, S.; Diercks, C. S.; Zhang, Y.-B.; Kornienko, N.; Nichols, E. M.; Zhao, Y.; Paris, A. Y.; Kim, D.; Yang, P.; Yaghi, O. M.; Chang, C. J. Covalent Organic Frameworks Comprising Cobalt Porphyrins for Catalytic CO_2 Reduction in Water. *Science* **2015**, *349*, 1208−1213.

(23) Meng, Z.; Luo, J.; Li, W.; Mirica, K. A. Hierarchical Tuning of the Performance of Electrochemical Carbon Dioxide Reduction Using Conductive Two-Dimensional Metallophthalocyanine Based Metal-Organic Frameworks. *J. Am. Chem. Soc.* **2020**, *142*, 21656−21669.

(24) An, S.; Lu, C.; Xu, Q.; Lian, C.; Peng, C.; Hu, J.; Zhuang, X.; Liu, H. Constructing Catalytic Crown Ether-Based Covalent Organic Frameworks for Electroreduction of CO_2. *ACS Energy Lett.* **2021**, *6*, 3496−3502.

(25) Evans, A. M.; Giri, A.; Sangwan, V. K.; Xun, S.; Bartnof, M.; Torres-Castanedo, C. G.; Balch, H. B.; Rahn, M. S.; Bradshaw, N. P.; Vitaku, E.; Burke, D. W.; Li, H.; Bedzyk, M. J.; Wang, F.; Brédas, J.-L.; Malen, J. A.; McGaughey, A. J. H.; Hersam, M. C.; Dichtel, W. R.; Hopkins, P. E. Thermally Conductive Ultra-Low-K Dielectric Layers Based on Two-Dimensional Covalent Organic Frameworks. *Nat. Mater.* **2021**, *20*, 1142−1148.

(26) Wang, M.; Wang, M.; Lin, H.-H.; Ballabio, M.; Zhong, H.; Bonn, M.; Zhou, S.; Heine, T.; Cánovas, E.; Dong, R.; Feng, X. High-Mobility Semiconducting Two-Dimensional Conjugated Covalent Organic Frameworks with *p*-Type Doping. *J. Am. Chem. Soc.* **2020**, *142*, 21622−21627.

(27) Wan, S.; Gándara, F.; Asano, A.; Furukawa, H.; Saeki, A.; Dey, S. K.; Liao, L.; Ambrogio, M. W.; Botros, Y. Y.; Duan, X.; Seki, S.; Stoddart, J. F.; Yaghi, O. M. Covalent Organic Frameworks with High Charge Carrier Mobility. *Chem. Mater.* **2011**, *23*, 4094−4097.

(28) Feng, X.; Liu, L.; Honsho, Y.; Saeki, A.; Seki, S.; Irle, S.; Dong, Y.; Nagai, A.; Jiang, D. High-Rate Charge-Carrier Transport in Porphyrin Covalent Organic Frameworks: Switching from Hole to Electron to Ambipolar Conduction. *Angew. Chem., Int. Ed.* **2012**, *124*, 2672−2676.

(29) Guo, J.; Xu, Y.; Jin, S.; Chen, L.; Kaji, T.; Honsho, Y.; Addicoat, M. A.; Kim, J.; Saeki, A.; Ihee, H.; Seki, S.; Irle, S.; Hiramoto, M.; Gao, J.; Jiang, D. Conjugated Organic Framework with Three-Dimensionally Ordered Stable Structure and Delocalized π Clouds. *Nat. Commun.* **2013**, *4*, 2736.

(30) Meng, Z.; Stolz, R. M.; Mirica, K. A. Two-Dimensional Chemiresistive Covalent Organic Framework with High Intrinsic Conductivity. *J. Am. Chem. Soc.* **2019**, *141*, 11929−11937.

(31) Abel, M.; Clair, S.; Ourdjini, O.; Mossoyan, M.; Porte, L. Single Layer of Polymeric Fe-Phthalocyanine: An Organometallic Sheet on Metal and Thin Insulating Film. *J. Am. Chem. Soc.* **2011**, *133*, 1203−1205.

(32) Wu, Y.; Liang, Y.; Wang, H. Heterogeneous Molecular Catalysts of Metal Phthalocyanines for Electrochemical CO_2 Reduction Reactions. *Acc. Chem. Res.* **2021**, *54*, 3149−3159.

(33) Lv, N.; Li, Q.; Zhu, H.; Mu, S.; Luo, X.; Ren, X.; Liu, X.; Li, S.; Cheng, C.; Ma, T. Electrocatalytic Porphyrin/Phthalocyanine-Based Organic Frameworks: Building Blocks, Coordination Microenvironments, Structure-Performance Relationships. *Adv. Sci.* **2023**, *10*, 2206239.

(34) Huang, S.; Chen, K.; Li, T.-T. Porphyrin and Phthalocyanine Based Covalent Organic Frameworks for Electrocatalysis. *Coord. Chem. Rev.* **2022**, *464*, 214563.

https://doi.org/10.1021/jacs.3c08594
J. Am. Chem. Soc. 2023, 145, 24230−24239

(35) Han, B.; Ding, X.; Yu, B.; Wu, H.; Zhou, W.; Liu, W.; Wei, C.; Chen, B.; Qi, D.; Wang, H.; Wang, K.; Chen, Y.; Chen, B.; Jiang, J. Two-Dimensional Covalent Organic Frameworks with Cobalt (II)-Phthalocyanine Sites for Efficient Electrocatalytic Carbon Dioxide Reduction. *J. Am. Chem. Soc.* **2021**, *143*, 7104−7113.
(36) Lu, M.; Zhang, M.; Liu, C.-G.; Liu, J.; Shang, L.-J.; Wang, M.; Chang, J.-N.; Li, S.-S.; Lan, Y.-Q. Stable Dioxin-Linked Metallophthalocyanine Covalent Organic Frameworks (COFs) as Photo-Coupled Electrocatalysts for CO_2 Reduction. *Angew. Chem., Int. Ed.* **2021**, *60*, 4864−4871.
(37) Sedghi, G.; García-Suárez, V. M.; Esdaile, L. J.; Anderson, H. L.; Lambert, C. J.; Martín, S.; Bethell, D.; Higgins, S. J.; Elliott, M.; Bennett, N.; Macdonald, J. E.; Nichols, R. J. Long-Range Electron Tunnelling in Oligo-Porphyrin Molecular Wires. *Nat. Nanotechnol.* **2011**, *6*, 517−523.
(38) Zhou, J.; Sun, Q. Magnetism of Phthalocyanine-Based Organometallic Single Porous Sheet. *J. Am. Chem. Soc.* **2011**, *133*, 15113−15119.
(39) Drinkard, W. C.; Bailar, J. C. Copper Phthalocyanine Polymers. *J. Am. Chem. Soc.* **1959**, *81*, 4795−4797.
(40) Epstein, A.; Wildi, B. S. Electrical Properties of Poly-Copper Phthalocyanine. *J. Chem. Phys.* **1960**, *32*, 324−329.
(41) Bannehr, R.; Meyer, G.; Wöhrle, D. Polymer Phthalocyanines and their Precursors 2. The Structure of Polyphthalocyanines. *Polym. Bull.* **1980**, *2*, 841−846.
(42) Chen, J.; Zou, K.; Ding, P.; Deng, J.; Zha, C.; Hu, Y.; Zhao, X.; Wu, J.; Fan, J.; Li, Y. Conjugated Cobalt Polyphthalocyanine as the Elastic and Reprocessable Catalyst for Flexible Li-CO_2 Batteries. *Adv. Mater.* **2019**, *31*, 1805484.
(43) Winslow, F. H.; Baker, W. O.; Yager, W. A. Odd Electrons in Polymer Molecules. *J. Am. Chem. Soc.* **1955**, *77* (18), 4751−4756.
(44) Kutzler, F. W.; Barger, W. R.; Snow, A. W.; Wohltjen, H. An Investigation of Conductivity in Metal-Substituted Phthalocyanine Langmuir-Blodgett Films. *Thin Solid Films* **1987**, *155*, 1−16.
(45) Yue, Y.; Li, H.; Chen, H.; Huang, N. Piperazine-Linked Covalent Organic Frameworks with High Electrical Conductivity. *J. Am. Chem. Soc.* **2022**, *144*, 2873−2878.
(46) Zhang, X.; Wang, Y.; Gu, M.; Wang, M.; Zhang, Z.; Pan, W.; Jiang, Z.; Lucero, M.; Wang, H.; Sterbinsky, G. E.; Ma, Q.; Wang, Y.-G.; Feng, Z.; Li, J.; Dai, H.; Liang, Y. Molecular Engineering of Dispersed Nickel Phthalocyanines on Carbon Nanotubes for Selective CO_2 Reduction. *Nat. Energy* **2020**, *5*, 684−692.
(47) Chen, K.; Cao, M.; Lin, Y.; Fu, J.; Liao, H.; Zhou, Y.; Li, H.; Qiu, X.; Hu, J.; Zheng, X.; Shakouri, M.; Xiao, Q.; Hu, Y.; Li, J.; Liu, J.; Cortés, E.; Liu, M. Nickel Ligand Engineering in Nickel Phthalocyanine to Boost the Electrocatalytic Reduction of CO_2. *Adv. Funct. Mater.* **2022**, *32*, 2111322.
(48) Zhang, W.; Chao, Y.; Zhang, W.; Zhou, J.; Lv, F.; Wang, K.; Lin, F.; Luo, H.; Li, J.; Tong, M.; Wang, E.; Guo, S. Emerging Dual-Atomic-Site Catalysts for Efficient Energy Catalysis. *Adv. Mater.* **2021**, *33*, 2102576.
(49) Zang, Y.; Lu, D.-Q.; Wang, K.; Li, B.; Peng, P.; Lan, Y.-Q.; Zang, S.-Q. A Pyrolysis-Free Ni/Fe Bimetallic Electrocatalyst for Overall Water Splitting. *Nat. Commun.* **2023**, *14*, 1792.
(50) Ren, W.; Tan, X.; Yang, W.; Jia, C.; Xu, S.; Wang, K.; Smith, S. C.; Zhao, C. Isolated Diatomic Ni-Fe Metal-Nitrogen Sites for Synergistic Electroreduction of CO_2. *Angew. Chem., Int. Ed.* **2019**, *58*, 6972−6976.
(51) Yao, D.; Tang, C.; Johannessen, B.; Slattery, A.; Chern, S.; Qiao, S.-Z. Inter-Metal Interaction with a Threshold Effect in NiCu Dual-Atom Catalysts for CO_2 Electroreduction. *Adv. Mater.* **2023**, *35*, 2209386.
(52) Li, W.-H.; Yang, J.; Wang, D. Long-Range Interaction on Diatomic Catalysts Boosting Electrocatalysis. *Angew. Chem., Int. Ed.* **2022**, *61*, No. e202213318.
(53) Zhu, Z.; Yin, H.; Wang, Y.; Chuang, C.-H.; Xing, L.; Dong, M.; Lu, Y.-R.; Casillas-Garcia, G.; Zheng, Y.; Chen, S.; Dou, Y.; Liu, P.; Chen, Q.; Zhao, H. Coexisting Single-Atomic Fe and Ni Sites on Hierarchically Ordered Porous Carbon as a Highly Efficient ORR Electrocatalyst. *Adv. Mater.* **2020**, *32*, 2004670.
(54) Dong, X.-Y.; Si, Y.-N.; Wang, Q.-Y.; Wang, S.; Zang, S.-Q. Integrating Single Atoms with Different Microenvironments into One Porous Organic Polymer for Efficient Photocatalytic CO_2 Reduction. *Adv. Mater.* **2021**, *33*, 2101568.
(55) Vorobiev, A. Magnetoplasma and Cyclotron Phenomena in the High-Temperature X-Band Electron Paramagnetic Resonance Spectra of Graphite. *J. Phys. Chem. C* **2023**, *127*, 4341−4350.
(56) Ye, S. Probing Electronic Structures of Transition Metal Complexes Using Electron Paramagnetic Resonance Spectroscopy. *Magnetic Resonance Letters* **2023**, *3*, 43−60.
(57) Zhang, Z.; Xiao, J.; Chen, X.-J; Yu, S.; Si, R.; Wang, Y.; Wang, S.; Meng, X.; Wang, Y.; Tian, Z.-Q.; Deng, D. Reaction Mechanisms of Well-Defined Metal-N_4 Sites in Electrocatalytic CO_2 Reduction. *Angew. Chem., Int. Ed.* **2018**, *57*, 16339−16342.
(58) Jiao, L.; Yang, W.; Wan, G.; Zhang, R.; Zheng, X.; Zhou, H.; Yu, S.-H.; Jiang, H.-L. Single-Atom Electrocatalysts from Multivariate Metal-Organic Frameworks for Highly Selective Reduction of CO_2 at Low Pressures. *Angew. Chem., Int. Ed.* **2020**, *59*, 20589−20595.
(59) Chen, C.; Sun, X.; Yan, X.; Wu, Y.; Liu, H.; Zhu, Q.; Bediako, B.; Han, B. Boosting CO_2 Electroreduction on N, P-Co-doped Carbon Aerogels. *Angew. Chem., Int. Ed.* **2020**, *132*, 11216−11222.
(60) Rendón-Calle, A.; Builes, S.; Calle-Vallejo, F. A brief review of the computational modeling of CO_2 electroreduction on Cu electrodes. *Curr. Opin. Electrochem.* **2018**, *9*, 158−165.
(61) Zhu, W.; Zhang, L.; Liu, S.; Li, A.; Yuan, X.; Hu, C.; Zhang, G.; Deng, W.; Zang, K.; Luo, J.; Zhu, Y.; Gu, M.; Zhao, Z.-J.; Gong, J. Enhanced CO_2 Electroreduction on Neighboring Zn/Co Monomers by Electronic Effect. *Angew. Chem., Int. Ed.* **2020**, *59*, 12664−12668.
(62) Hammer, B.; Hansen, L. B.; Nørskov, J. K. Improved Adsorption Energetics within Density-Functional Theory Using Revised Perdew-Burke-Ernzerhof Functionals. *Phys. Rev. B* **1999**, *59*, 7413−7421.

https://doi.org/10.1021/jacs.3c08594
J. Am. Chem. Soc. 2023, 145, 24230−24239